

Highlights

Rediscovering Hyperelasticity by Deep Symbolic Regression

Rasul Abdusalamov, Mikhail Itskov

- Proposed novel hyperelastic material models discovered through deep symbolic regression from experimental data eliminating human bias in model selection
- Successfully fitted classical Treloar and Kawabata data sets with interpretable strain energy functions requiring few material parameters
- Demonstrated that utilizing both the first and second invariants is crucial for accurately capturing complex behavior of rubber-like materials under diverse loading conditions

Rediscovering Hyperelasticity by Deep Symbolic Regression

Rasul Abdusalamov^{a,*,1}, Mikhail Itskov^{a,b,2}

^aDepartment of Continuum Mechanics, RWTH Aachen University, Eilfschornsteinstr. 18, Aachen, 52062, NRW, Germany

^bSchool of Computer Science & Mathematics, Keele University, ST5 5BG, Staffordshire, United Kingdom

ARTICLE INFO

Keywords:

Hyperelasticity

Material Modeling

Deep Symbolic Regression

Machine Learning

ABSTRACT


The accurate modeling of the mechanical behavior of rubber-like materials under multi-axial loading constitutes a long-standing challenge in hyperelastic material modeling. This work employs deep symbolic regression as an interpretable machine learning approach to discover novel strain energy functions directly from experimental results, with a specific focus on the classical Treloar and Kawabata data sets for vulcanized rubber. The proposed approach circumvents traditional human model selection biases by exploring possible functional forms of strain energy functions, expressed in terms of both the first and second principal invariants of the right Cauchy-Green tensor. The resulting models exhibit high predictive accuracy for various deformation modes, including uniaxial tension, pure shear, equal biaxial tension, and biaxial loading. This work underscores the potential of deep symbolic regression in advancing hyperelastic material modeling and highlights the importance of considering both invariants in capturing the complex behaviors of rubber-like materials.


1. Introduction

When conducting finite element (FE) simulations with the aim of predicting the mechanical behavior of materials under various loading conditions, it is essential to employ constitutive models of the highest possible accuracy. This is particularly true in the case of elastomeric materials subjected to large deformations. In literature, numerous hyperelastic models have been proposed for elastomers. However, not all of them are capable of reproducing the complete mechanical behavior across different loading types and for a wide range of different rubber-like materials. This situation often poses a significant challenge to engineers in selecting the most appropriate model with minimal number of material parameters. A comprehensive review of the literature pertaining to hyperelastic materials models and their functionality is provided in a series of papers, including those by Marckmann and Verron (2006); Xiang, Zhong, Rudykh, Zhou, Qu and Yang (2020); Melly, Liu, Liu and Leng (2021); Dal, Açıköz and Badienia (2021); He, Zhang, Zhang, Chen, Zhang and Li (2022); Ricker and Wriggers (2023) and numerous references therein. In recent years, a considerable number of additional material models have been introduced, with a notable emphasis on highly specialized materials and the identification of specific effects. A number of approaches have been developed which focus, for example, on micro-mechanically based constitutive models (Itskov and Knyazeva, 2016; Khiêm and Itskov, 2017; Mirzapour, 2023), interpolation-based approaches for phenomenological constitutive models (Meng, Imtiaz and Liu, 2021) or even strain-mode-dependent concepts (Mahnken, 2022). A critical evaluation of the existing modeling approaches reveals several drawbacks. Firstly, the calibration of material models is often challenging due to the necessity of multiple material parameters. Secondly, many models exhibit constrained predictive accuracy in specific loading scenarios, attributable to the nature of input data and assumptions made during model development. Thirdly, implementing each model as a user material model in commercial FE solvers necessitates a substantial investment of time. Fourthly, all of the aforementioned models have been developed by humans, which introduces a potential bias into the model structure and consequently results in a limitation of predictive capabilities. For these reasons, a more sophisticated approach is necessary, capable of generating specific material models while maintaining reasonable computation time without the need for extensive expert knowledge. Furthermore, the approach must be implementable for practical use in industrial applications.

Some of these limitations can be circumvented by employing data-driven techniques. With the advancement of machine learning, numerous data-driven modeling approaches have recently been developed for constitutive modeling of

*Corresponding author

 abdusalamov@km.rwth-aachen.de (R. Abdusalamov); itskov@km.rwth-aachen.de (M. Itskov)

 www.km.rwth-aachen.de (R. Abdusalamov); www.km.rwth-aachen.de (M. Itskov)

ORCID(s): 0000-0003-4988-4794 (R. Abdusalamov)

materials. Detailed reviews of such approaches can be found e.g. in Herrmann and Kollmannsberger (2024) and Fuhg, Padmanabha, Bouklas, Bahmani, Sun, Vlassis, Flaschel, Carrara and Lorenzis (2024). They include physics-augmented neural networks (Kalina, Linden, Brummund and Kästner, 2023), polyconvex anisotropic hyperelasticity with neural networks (Klein, Fernández, Martin, Neff and Weeger, 2022), discovery of material models using sparse regression (Flaschel, Kumar and De Lorenzis, 2023), model-free approaches (Kirchdoerfer and Ortiz, 2016), constitutive artificial neural networks (Linka, Hillgärtner, Abdolazizi, Aydin, Itskov and Cyron, 2021), and constitutive Kolmogorov–Arnold networks (Abdolazizi, Aydin, Cyron and Linka, 2025). Many of these concepts introduce theoretical knowledge from materials theory or thermodynamics into the frameworks and focus on invariant-based or strain-based approaches. Despite their advantages, these methods are not without their limitations. While artificial neural networks offer significant benefits in terms of model discovery, they are often regarded as "black boxes", which poses a substantial challenge to interpretation and usage in industrial applications. Furthermore, the training of such models necessitates substantial computational effort, and the high complexity of the resulting models can hinder further applications, such as FE simulations. In addressing these limitations, efforts have been made to enhance interpretability within the methods and to significantly reduce the complexity of the neural networks (see, e.g. (Linka and Kuhl, 2023)). Whilst this approach enhances interpretability, it is a process of adjusting model coefficients through fitting weights and biases of a neural network. An alternative approach could be to employ a conventional nonlinear optimization scheme that would not necessitate a complex neural network architecture. Furthermore, many of the presented methods do not lead to the discovery of novel material models. The identification of a most appropriate combination of already known terms from a given set of functions closely aligned with the underlying data remains the primary objective. A further drawback is that many approaches combine redundant inputs such as invariants and principal stretches (see, e.g. Abdolazizi et al. (2025)).

An alternative method that has been demonstrated to overcome many of the disadvantages of neural networks is symbolic regression (SR). Symbolic regression is a relatively novel regression method that belongs to the class of interpretable machine learning algorithms. It determines a mathematical expression by searching a solution space where the best-fitting expression structure is identified for a given data set (Augusto and Barbosa, 2000). Accordingly, an expression that is optimal in terms of simplicity and accuracy with respect to the data set is formulated. The principal benefit of this approach is that it identifies an analytical model while reducing the effect of human bias. Recent applications include the development of interpretable hyperelastic material models (Abdusalamov, Hillgärtner and Itskov, 2023), plasticity models (Bomarito, Townsend, Stewart, Esham, Emery and Hochhalter, 2021), modeling the Mullins effect (Abdusalamov, Weise and Itskov, 2024), and learning implicit yield surface models using uncertainty quantification (Birky, Emery, Hamel and Hochhalter, 2025). Furthermore a novel method for constitutive law discovery that relies on formal grammars and shares notable similarities with a symbolic regression approach has recently been proposed (Kissas, Mishra, Chatzi and De Lorenzis, 2024).

Extending the work presented in Abdusalamov et al. (2024) we employ here deep symbolic regression as an interpretable machine learning approach to discover novel strain energy functions directly from experimental data. In particular, we focus on the classical Treloar and Kawabata data sets for vulcanized rubber. The proposed approach circumvents traditional human model selection biases by exploring possible strain energy functions. The resulting models demonstrate high levels of predictive accuracy across various deformation modes, including uniaxial tension, pure shear and biaxial tension.

The structure of the paper is as follows: Section 2 discusses the proposed methodology, including an overview of deep symbolic regression embedded into a continuum mechanical framework. Section 3 presents the results for the newly discovered strain energy functions for the Treloar and Kawabata data sets. Additionally, the robustness of the presented approach is evaluated with respect to noise. Furthermore, a stretch-based approach is discussed. Finally, a brief conclusion highlights the main aspects of this work in Section 4.

2. Methodology

2.1. Continuum Mechanical Framework

A strain energy function $\Psi(\mathbf{C})$ of an isotropic hyperelastic material can be expressed in terms of the principal invariants $I_{\mathbf{C}}$, $II_{\mathbf{C}}$ and $III_{\mathbf{C}}$ of the right Cauchy-Green tensor $\mathbf{C} = \mathbf{F}^T \mathbf{F}$, where \mathbf{F} denotes the deformation gradient. Consequently, the first Piola-Kirchhoff stress tensor \mathbf{P} can be expressed as follows:

$$\mathbf{P} = 2\mathbf{F} \frac{\partial \Psi(\mathbf{C})}{\partial \mathbf{C}} = 2 \left[\left(\frac{\partial \Psi}{\partial I_{\mathbf{C}}} + I_{\mathbf{C}} \frac{\partial \Psi}{\partial II_{\mathbf{C}}} \right) \mathbf{F} - \frac{\partial \Psi}{\partial II_{\mathbf{C}}} \mathbf{F} \mathbf{C} + III_{\mathbf{C}} \frac{\partial \Psi}{\partial III_{\mathbf{C}}} \mathbf{F}^{-T} \right]. \quad (1)$$

It is important to highlight that the impact of the material is solely determined by the terms marked **blue**. The invariants $I_{\mathbf{C}}$, $\Pi_{\mathbf{C}}$ and $\text{III}_{\mathbf{C}}$ of \mathbf{C} are given by

$$I_{\mathbf{C}} = \text{tr } \mathbf{C}, \quad \Pi_{\mathbf{C}} = \frac{1}{2} [(\text{tr } \mathbf{C})^2 - \text{tr } (\mathbf{C}^2)], \quad \text{and} \quad \text{III}_{\mathbf{C}} = \det \mathbf{C}. \quad (2)$$

$\Psi(\mathbf{C})$ satisfies the conditions of the energy and stress-free natural state at $\mathbf{F} = \mathbf{I}$ given by

$$\Psi(\mathbf{I}) = 0 \quad \text{and} \quad \left. \frac{\partial \Psi(\mathbf{C})}{\partial \mathbf{C}} \right|_{\mathbf{C}=\mathbf{I}} = \mathbf{0}. \quad (3)$$

In the case of nearly incompressible behavior, it is common to multiplicatively decompose the deformation gradient into a volumetric $\hat{\mathbf{F}} = J\mathbf{I}$ and an isochoric part $\bar{\mathbf{F}} = J^{-1/3}\mathbf{F}$, where $J = \det \mathbf{F} = \sqrt{\text{III}_{\mathbf{C}}}$ (see (Richter, 1948) for further details). Consequently, the principal invariants of the isochoric right Cauchy-Green tensor $\bar{\mathbf{C}} = \bar{\mathbf{F}}^T \bar{\mathbf{F}}$ take the form

$$I_{\bar{\mathbf{C}}} = J^{-2/3}I_{\mathbf{C}}, \quad \Pi_{\bar{\mathbf{C}}} = J^{-4/3}\Pi_{\mathbf{C}} \quad \text{and} \quad \text{III}_{\bar{\mathbf{C}}} = 1. \quad (4)$$

Accordingly, the first Piola-Kirchhoff stress tensor can be expressed as

$$\mathbf{P} = 2 \left(\frac{\partial \Psi}{\partial I_{\bar{\mathbf{C}}}} + I_{\bar{\mathbf{C}}} \frac{\partial \Psi}{\partial \Pi_{\bar{\mathbf{C}}}} \right) J^{-2/3} \mathbf{F} - 2 \frac{\partial \Psi}{\partial \Pi_{\bar{\mathbf{C}}}} J^{-4/3} \mathbf{F} \mathbf{C} + J \left(\frac{\partial \Psi}{\partial J} - \frac{2}{3J} \frac{\partial \Psi}{\partial I_{\bar{\mathbf{C}}}} I_{\bar{\mathbf{C}}} - \frac{4}{3J} \frac{\partial \Psi}{\partial \Pi_{\bar{\mathbf{C}}}} \Pi_{\bar{\mathbf{C}}} \right) \mathbf{F}^{-T}. \quad (5)$$

In the case of incompressible materials, characterized by the constraint $J = 1$, the constitutive equation will take the following form:

$$\mathbf{P} = 2\mathbf{F} \frac{\partial \Psi(\mathbf{C})}{\partial \mathbf{C}} - p\mathbf{F}^{-T} = 2 \left[\left(\frac{\partial \Psi}{\partial I_{\mathbf{C}}} + I_{\mathbf{C}} \frac{\partial \Psi}{\partial \Pi_{\mathbf{C}}} \right) \mathbf{F} - \frac{\partial \Psi}{\partial \Pi_{\mathbf{C}}} \mathbf{F} \mathbf{C} \right] - p\mathbf{F}^{-T}, \quad (6)$$

where p denotes an arbitrary parameter related to the hydrostatic pressure. While the proposed formulations use strain invariants, it is also feasible to express the strain energy function Ψ in terms of the principal stretches $\lambda_i (i = 1, 2, 3)$. Then, in the case of distinct λ_i we can write

$$\mathbf{P} = \sum_{i=1}^3 \frac{\partial \Psi(\lambda_1, \lambda_2, \lambda_3)}{\partial \lambda_i} \mathbf{n}_i \otimes \mathbf{N}_i, \quad (7)$$

where \mathbf{n}_i and \mathbf{N}_i are unit eigenvectors of $\mathbf{b} = \mathbf{F}\mathbf{F}^T$ and \mathbf{C} , respectively.

According to the Valanis-Landel concept, the strain-energy density function Ψ of a hyperelastic material can be expressed in terms of a continuously differentiable function ω as follows (Valanis and Landel, 1967)

$$\Psi(\lambda_1, \lambda_2, \lambda_3) = \omega(\lambda_1) + \omega(\lambda_2) + \omega(\lambda_3). \quad (8)$$

The above mentioned conditions of the zero energy and stress free reference state require that

$$\omega(1) = 0 \quad \text{and} \quad \omega'(1) = 0. \quad (9)$$

Within the proposed framework of deep symbolic regression, both the invariant and stretch based formulation can be used to identify strain energy functions that describe an specified data set. The well-known Ogden model represents a special case of (8) with

$$\Psi(\lambda_1, \lambda_2, \lambda_3) = \sum_{i=1}^N \frac{\mu_i}{\alpha_i} (\lambda_1^{\alpha_i} + \lambda_2^{\alpha_i} + \lambda_3^{\alpha_i} - 3), \quad (10)$$

It gained wide acceptance in industrial FE software and has demonstrated excellent performance (Ogden, 1972).

2.2. Deep Symbolic Regression

The deep symbolic regression package developed by [Petersen, Landajuela, Mundhenk, Santiago, Kim and Kim \(2021\)](#) utilizes a recurrent neural network (RNN) to predict a mathematical expression based on a sampled distribution through a risk-seeking policy gradient. The framework is principally based on a reinforcement learning approach. Each expression tree is transformed into a sequence, referred to as a traversal, which corresponds to the environment of the reinforcement learning task (see [Figure 1](#)). The node values of the traversal referred to as tokens, represent either operations, functions, constants, or arguments. The recurrent neural network, serving as the agent is trained iteratively on a hierarchical input containing information about the entire expression tree. The traversal is decomposed into observations about siblings and parents fed directly into the RNN. The next element of the traversal, corresponding to the action, is sampled based on a probability distribution function. A reward function is formulated based on the performance of the sampled expression on the given data set. The detailed process of the RL algorithm is illustrated for example by the strain energy function $\Psi(\mathbf{I}_C, \mathbf{II}_C) = \mathbf{I}_C + 0.5 \ln(\mathbf{II}_C)$ (see [Figure 1](#)) and proceeds as follows:

1. In each epoch, a batch of expressions is sampled according to the following steps:
 - i. In the initialization phase the sampling of an initial token (the root of the expression tree) from a library containing all the necessary operations, functions, constants, and arguments takes place. The sampling of the token is derived from a predefined probability distribution. This initial step does not specify any information about parent or sibling relationships. In the illustrated example, the first sampled token in the first iteration represents the addition operator $+$.
 - ii. Sampling of subsequent tokens requires update of observations based on the previous token, the updating of the weights of the RNN, and the sampling of the next token. An advantage of this approach is that search space constraints can be incorporated directly into the sampling process, which can be achieved by introducing a prior into the probability distribution function. One such a prior constraint on the search space is that all children of an operator cannot be constants, given that they would otherwise be reduced to another constant. For instance, in the second iteration of the subsequent sampling step, the addition operator is designated as the parent with an arity of two, since there are no siblings and no additional information is specified. Thus, the first input \mathbf{I}_C is the next sampled token.
 - iii. This iterative process is continued as long as all nodes in the tree have been assigned a terminal node status, which is either a constant or an input variable. In this manner, each token within the expression for $\Psi(\mathbf{I}_C, \mathbf{II}_C)$ is sampled in a stepwise manner until an expression is determined.
2. Based on the generation of expressions, the reward is calculated using the normalized root mean square error (NRMSE). A risk-seeking policy gradient is implemented with the objective of maximizing the performance of a specified fraction of the best samples. Consequently, the best case performance is prioritized, albeit at the potential expense of lower worst case and average performance.

Furthermore, a prior is embedded into the sampled probability distribution. The prior is a valuable tool for constraining the search space, for example, by limiting specific sampling sequences. Furthermore, the DSO package offers a constant optimization option. Despite the increased time requirement and a certain risk of overfitting, this approach allows for a significantly higher rate of the expression recovery. Once a prior has been sampled, the corresponding symbolic expression is instantiated and evaluated. In this work, the following basis functions for the strain energy are provided: ["add", "sub", "n2", "mul", "div", "sqrt", "exp", "log"]. The normalization for the strain energy, as given by condition (3)₁ can easily be satisfied by correction of the resulting expression by a constant, which has been omitted in the following. Condition (3)₂ is fulfilled automatically by including the point $\mathbf{P} = \mathbf{0}$ at $\mathbf{F} = \mathbf{I}$ into the set of the data used for the search of the mathematical expression of the strain energy function.

3. Results and Discussion

In the following we apply deep symbolic regression to experimental data by [Treloar \(1944\)](#) and [Kawabata, Matsuda, Tei and Kawai \(1981\)](#) from uniaxial and biaxial tests of a vulcanized rubber. Fitting these classical data sets remains a significant challenge in hyperelastic material modeling. It is also a critical step towards a deeper understanding of the complex behavior of rubber-like materials under diverse deformation modes.

3.1. Multi-Axial Loading of Vulcanized Rubber

First the DSO package is employed to identify an optimal strain energy function for describing the Treloar data set from pure shear (PS), uniaxial (UT) and equibiaxial tension (EBT) tests. This data set has become one of the most

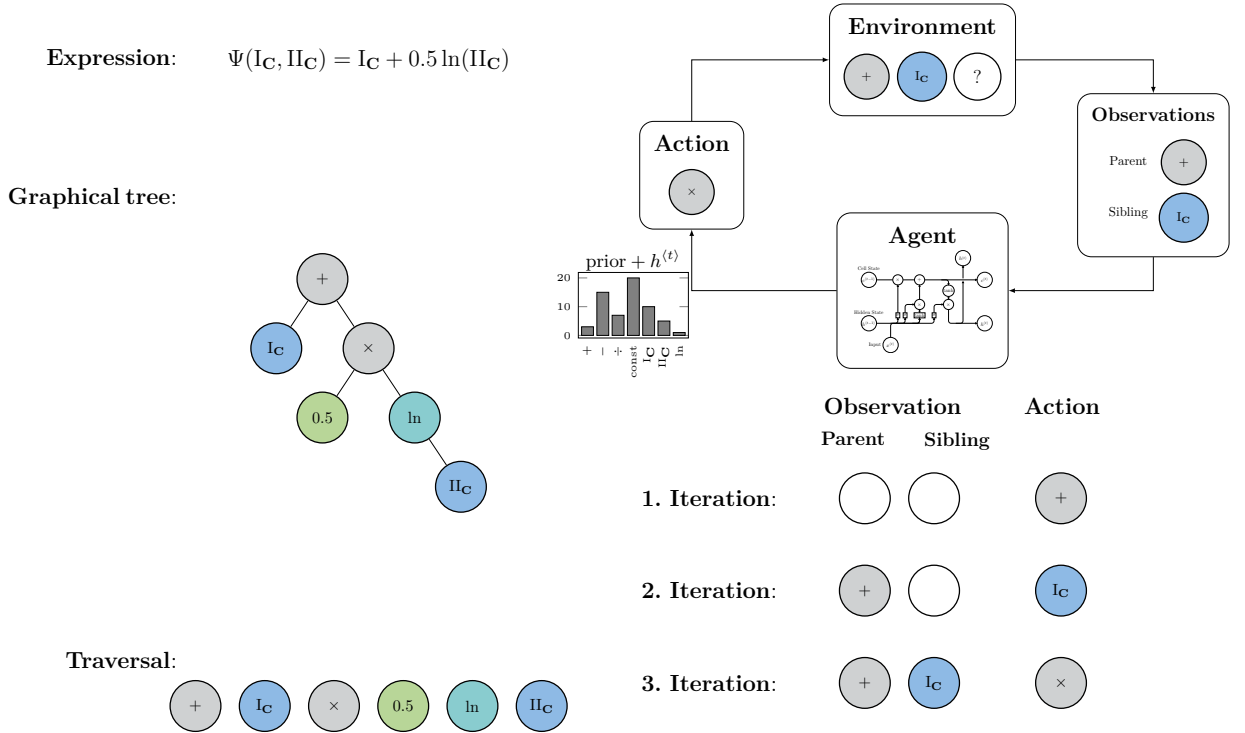


Figure 1: Expression sampling process of the deep symbolic regression framework applied to derive the strain energy function $\Psi(I_C, II_C) = I_C + 0.5 \ln(II_C)$. The RNN samples tokens given by operations, functions, constants inputs to build an expression tree starting from a root token. The rewards are computed using the NRMSE to train the RNN using a risk-seeking policy gradient.

well-known and frequently utilized benchmark tests for hyperelastic models, see e.g. [Ricker and Wriggers \(2023\)](#); [He et al. \(2022\)](#); [Marckmann and Verron \(2006\)](#) as well as references therein. All the models proposed in literature have been motivated by human bias to describe the underlying data. The question remains as to whether alternative unbiased model structures exist that could describe the data set more effectively with fewer parameters.

In the following, the data is divided into a training (80.00 %) and a test set (20.00 %). Subsequently, the efficacy of the identified strain energy functions is evaluated in comparison to these best established models, as referenced in ([Marckmann and Verron, 2006](#); [Ricker and Wriggers, 2023](#); [He et al., 2022](#)). To identify an appropriate material model, it is necessary to fit all three curves by [Treloar \(1944\)](#) simultaneously. The data set contains 14 data points for the EBT, 14 data points for the PS, and 25 data points for the UT response. Given the significant difference in the number of data points for EBT and UT, a straightforward approach is to duplicate the data set and assign a greater weight to the EBT response. This procedure is applied to all fits for all models compared. The best performing strain energy Ψ_T discovered is given by

$$\Psi_T = \underbrace{0.13I_C}_{\Psi_1} + \underbrace{2.40 \times 10^{-3}II_C}_{\Psi_2} + \underbrace{2.00 \times 10^{-3} \exp \sqrt{I_C}}_{\Psi_3} + \underbrace{2.76 \times 10^{-2} \left((\ln I_C)^2 + (\ln II_C)^2 \right)}_{\Psi_4}. \quad (11)$$

It demonstrates a high degree of predictive power, as evidenced by an R^2 score of 97.32%. [Figure 2](#) illustrates the UT, PS, and EBT responses of this hyperelastic model. Interestingly, strain energy function (11) can be split up into four additive terms. Separate contributions of these terms under UT, PS and EBT are illustrated in [Figure 3](#) and [Figure 4](#) for the whole and moderate range of deformations, respectively. The first basic term Ψ_1 represents the neo-Hookean model resulting from Gaussian chain statistics of polymer chains and is thus physically motivated. This term plays a pivotal role in the UT and PS responses, particularly within the range of small strains up to 300.00%. Ψ_2 belongs to the well-known Mooney-Rivlin model and appears to be particularly significant for strains exceeding 300.00%, resulting

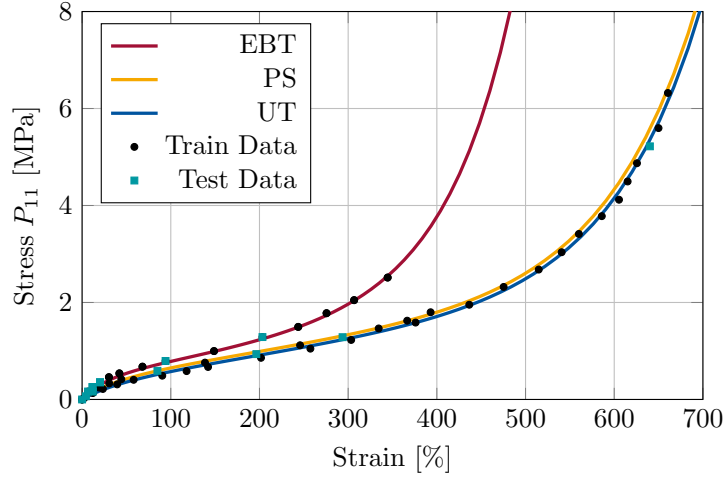


Figure 2: Best fit for the Treloar data set of novel model discovered through DS0. The stress-strain responses for UT, PS and EBT are generated from the strain energy function given in Equation 11.

in a markedly more rigid response in the EBT response. The contribution of Ψ_3 is of particular significance for all loading cases when the strain range exceeds 300.00%. The last term Ψ_4 becomes especially important under EBT response for the strain range between 0.00% and 300.00%.

Rivlin and Saunders (1951) observed in their experiments with a comparable rubber that $\partial\Psi/\partial I_C$ in the strain energy function Ψ is independent of both I_C and II_C , while $\partial\Psi/\partial II_C$ is independent of I_C and decreases with increasing II_C . In light of these observations, they proposed a strain energy function of the form:

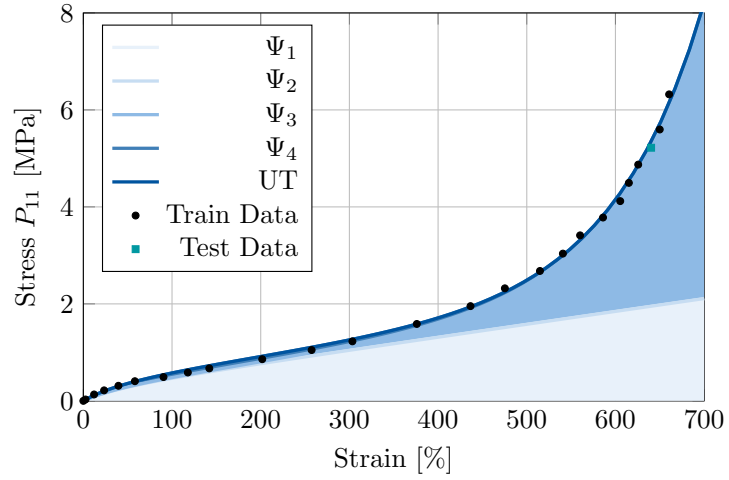
$$\Psi_T = c_{10} (I_C - 3) + \Phi (II_C - 3), \quad (12)$$

where c_{10} represents a constant, while Φ denotes a differentiable concave function. Based on this work, Gent and Thomas (1958) proposed Φ in the form

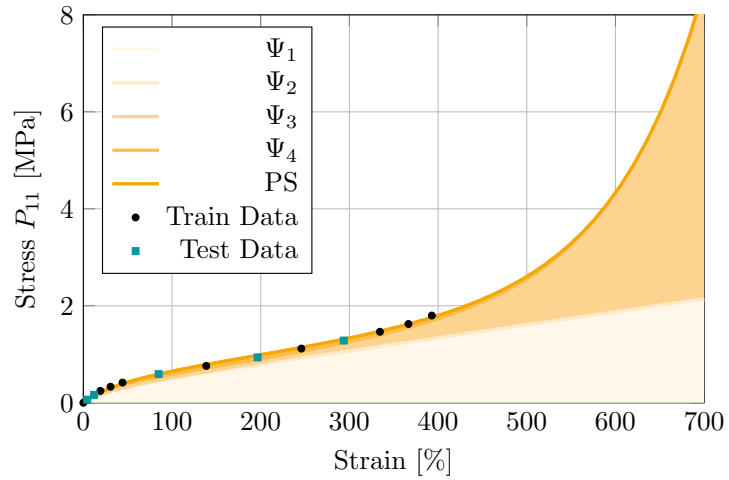
$$\Phi = c_{01} \ln \left(\frac{II_C}{3} \right), \quad (13)$$

where c_{01} is a constant. The strain energy function (11) appears to reflect this underlying logic, as evidenced by the term Ψ_4 . However, Ψ_4 is markedly more intricate and nonlinear in character than the classical models proposed for Φ . It is a considerable challenge for human intuition to successfully identify such a contribution. This term has a significant impact on the EBT response, while its influence under UT and PS is negligible.

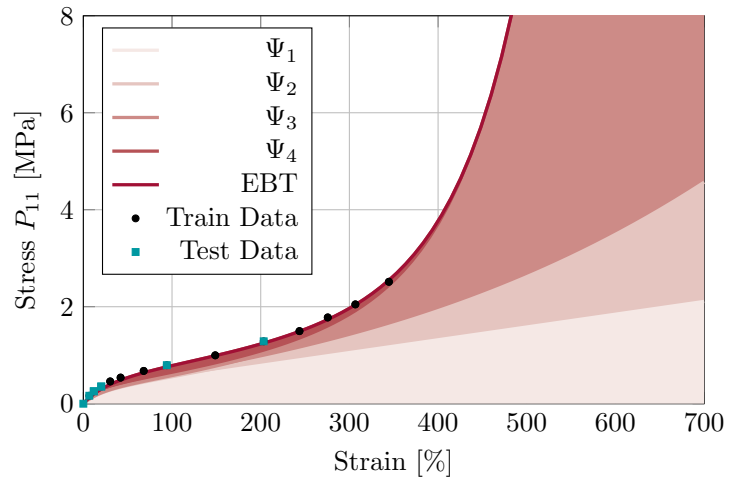
The found material model (11) is a more accurate representation of the data set than many traditional hyperelastic models and requires only four material constants. Marckmann and Verron (2006) provided a summary and comparative analysis of twenty different models based on their ability to fit the experimental data for the Treloar data set. It was observed that the extended-tube model with only four material parameters exhibited the best performance characteristics among all the models under consideration (Kaliske and Heinrich, 1999). Furthermore, the findings indicated that the non-hyperelastic Shariff and the unit sphere models demonstrated a high level of accuracy (Shariff, 2000; Miehe, Göktepe and Lulei, 2004). The three-terms Ogden model is extensively utilized in FE simulations and accurately describes the underlying experimental data. However, determination of its six material parameters necessitates a substantial experimental data set for precise fitting. The responses of these three models are illustrated in Figure 5. Models with fewer parameters, such as the three-chain, Hart-Smith, and eight-chain models are unable to accurately predict the stress response over the entire strain range and are not used for comparisons with the proposed strain energy function. Note that according to Marckmann and Verron (2006) for moderate strains of up to 200.00% - 250.00%, the two-parameter Mooney-Rivlin model demonstrated the greatest efficacy, exhibiting performance characteristics comparable to those of more complex models. For small strains up to 150.00%, the neo-Hookean model is the preferred choice due to its physical basis, simplicity with a single parameter, and ability to predict material response over a range of deformations modes. These conclusions are supported by the identified strain energy function



(a)

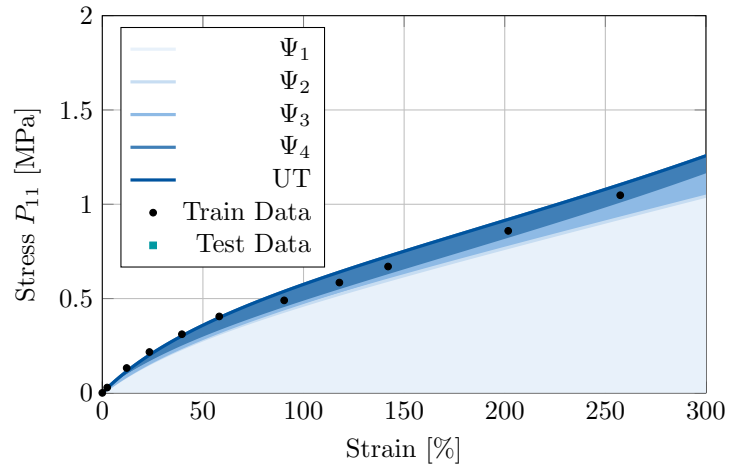


(b)

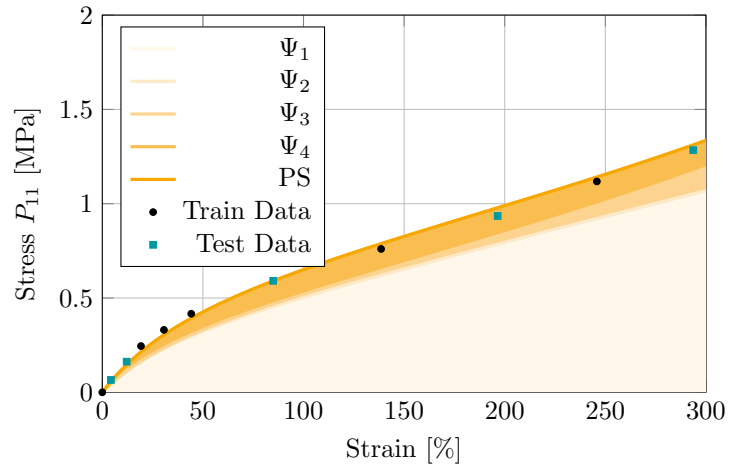


(c)

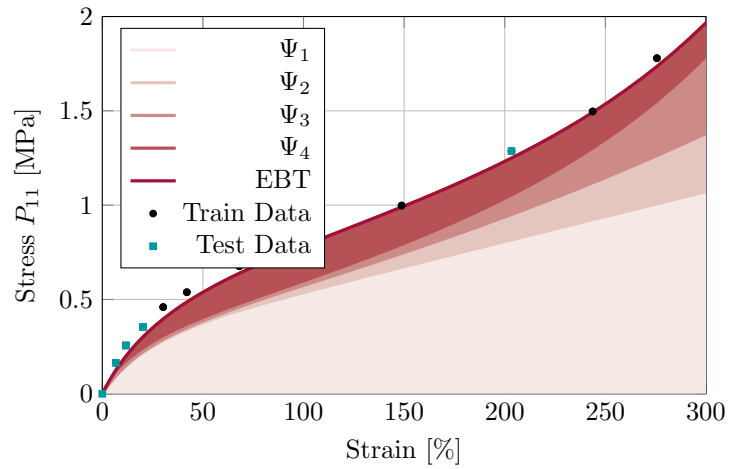
Figure 3: Visualization of the contributions of each term Ψ_i for $i = 1, \dots, 4$ in the strain energy (11). The responses are shown for UT, PS and EBT for the strain range from 0.00% to 700.00%.



(a)

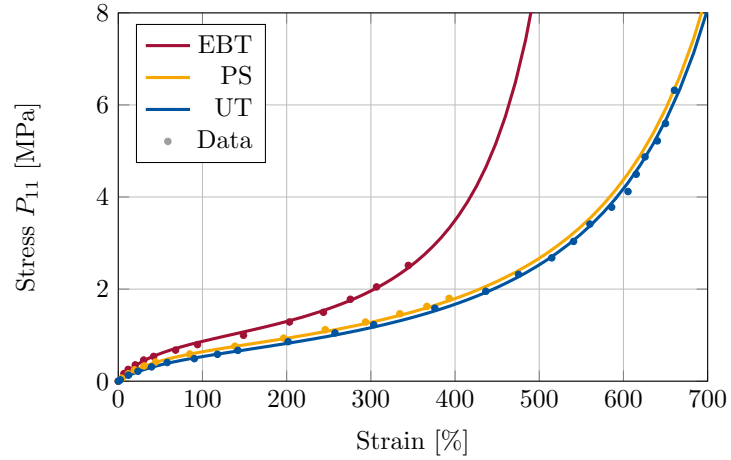


(b)

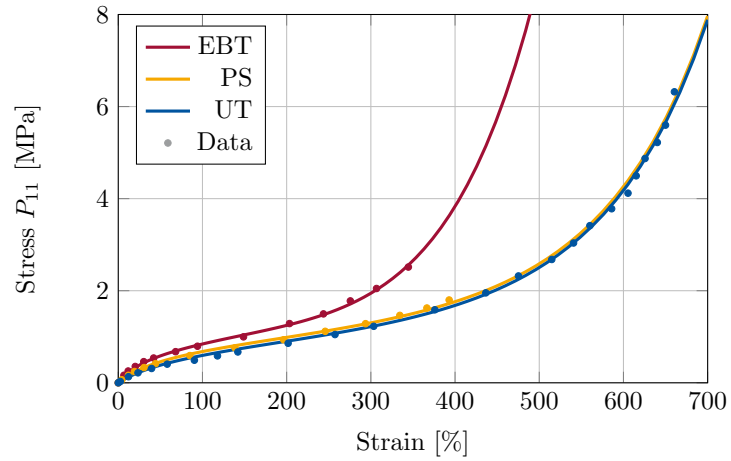


(c)

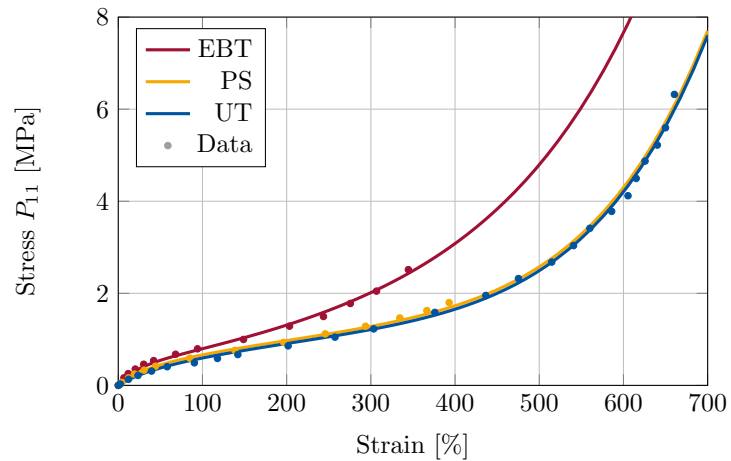
Figure 4: Visualization of the contributions of each term Ψ_i for $i = 1, \dots, 4$ in the strain energy (11). The responses are shown for UT, PS and EBT for the strain range from 0.00% to 300.00%.



(a)



(b)



(c)

Figure 5: Best fit for the Treloar data set using (a) the extended tube model ($R^2 = 96.56\%$), (b) the non-hyperelastic Shariff model ($R^2 = 96.38\%$) and (c) the stretch-based Ogden model ($R^2 = 95.58\%$) for UT, PS and EBT. The used material parameters are listed in Table 2, Table 3 and Table 4, respectively.

Table 1

Comparison of our novel model with existing approaches, showing the number of material constants and the R^2 score for the Treloar data for each model.

Model	Number of material constants	R^2 score
DSO	4	97.32 %
Extended tube model	4	96.56 %
Non-hyperelastic Shariff	5	96.38 %
Ogden model	6	95.58 %

Table 2

Material parameters of the extended tube model for the Treloar data set.

G_c	G_e	β	δ
0.20 MPa	0.19 MPa	0.34	0.10

Table 3

Material parameters of the non-hyperelastic Shariff model for the Treloar data set.

E	α_0	α_1	α_2	α_3	α_4
1.17 MPa	1.00	8.65×10^{-1}	3.66×10^{-2}	8.35×10^{-5}	2.04×10^{-2}

Table 4

Material parameters of the Ogden model for the Treloar data set.

	$i = 1$	$i = 2$	$i = 3$
α_i	1.74	7.28	-1.82
μ_i	4.13×10^{-1} MPa	1.22×10^{-5} MPa	-2.03×10^{-2} MPa

(11). The terms Ψ_1 and Ψ_2 serve as the fundamental building blocks for the neo-Hookean constitutive equation and the two-parameter Mooney-Rivlin model. As illustrated in Figure 4, these contributions are most significant for the small and moderate strain ranges up to 250.00 %.

Additionally, Ricker and Wriggers (2023) conducted a comprehensive study in which they fitted and compared a range of hyperelastic models for nine distinct rubber compounds, in addition to evaluating how these models performed when applied to the classical Treloar data set. It was concluded that across different rubber compounds, models with three to five parameters generally perform best. The investigation focused on identifying the role and importance of the second principal invariant for rubber models. According to the mentioned study UT is mainly influenced by I_C , while EBT and PS responses are equally affected by both I_C and II_C . Consequently, test data from a single experiment cannot adequately calibrate models dependent on both invariants. Furthermore, I_C -based models results in an underestimation of the EBT response. By incorporating additionally II_C , it is possible to achieve a balance in the stress response across diverse deformation modes and to offset potential limitations. These findings substantiate the observations made with the material model (11) predicted by DSO. A significant benefit of the proposed methodology is that it does not necessitate an initial screening of any models, thereby preventing any potential bias in the model selection. Constitutive relations can be directly identified from the specified data and inputs.

3.2. Influence of Noise

To study the quality of the data set provided and its impact on the performance of the obtained models we consider two distinct levels of noise

$$n_i(\lambda) = a_i \frac{\lambda}{\lambda_{\max}} \mathcal{N}(0, 1) \quad (14)$$

imposed on the experimental data, where $\mathcal{N}(0, 1)$ represents the normal distribution, a_i denotes the amplitude level, λ and λ_{\max} are the current and the maximal stretch, respectively. Accordingly, the noise level is proportional to the amplitude, the current strain, and is normalized to the maximum stretch.

The aim of this study is to determine whether the derived strain energy function is a unique solution and to explore the robustness of the prediction in the presence of noise. We examined two distinct amplitude levels $a_1 = 0.025$ MPa and $a_2 = 0.05$ MPa and found the following strain energy functions, respectively

$$\Psi_T^{n_1} = \frac{\ln I_C + 28.42}{-0.03I_C + 1.13 - \frac{1}{I_C} 19.64 \exp\left(7.57 \exp\left(0.02\sqrt{I_C} - \frac{1}{\sqrt{I_C}}\right) - 16.15\right)}, \quad (15)$$

$$\Psi_T^{n_2} = 0.09I_C + 0.11\sqrt{II_C} + 0.11 \exp\left(0.60\sqrt{0.75II_C - 1}\right) + \exp\left(0.07 \exp\left[\exp\left(0.02I_C\right)\right]\right). \quad (16)$$

For illustrative purposes, the stress-strain response for both models is presented in [Figure 6](#). In particular, the strain energy function corresponding to the first noise level is observed to accurately describe both the PS and UT responses. However, it is noted that the EBT response is slightly underestimated. Despite this discrepancy, the derived model captures the underlying data set with a high accuracy and a R^2 score of 98.19%. The second noise level formulation exhibits comparable patterns of behavior where the level of accuracy is given by a R^2 score of 97.15%. In this instance, the PS and UT responses demonstrate a high degree of similarity, while the EBT response is subject to an underestimation. This may be attributed to the occurrence of data overlap within the strain range of 0.00% to 200.00%, which is a direct result of the noise. Furthermore, this data overlap appears to result in a noticeably softer PS response in comparison to the first noise level for strains over 300.00%.

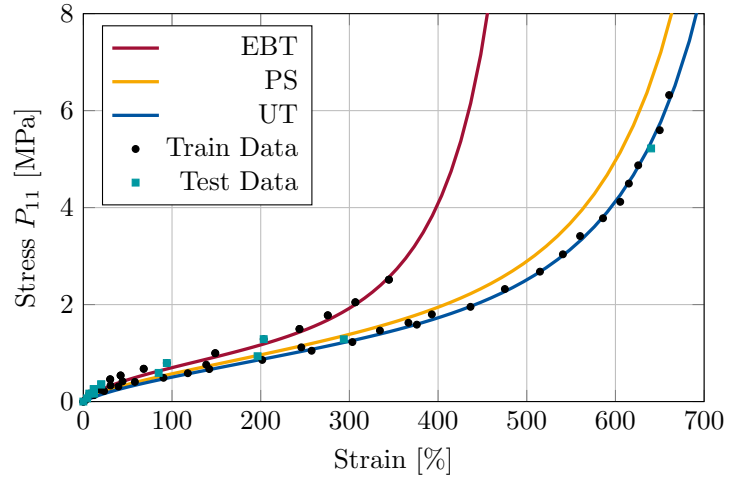
This investigation demonstrates the significance of accurate experimental data. Additionally, the results indicate multiplicity of solutions for the strain energy function capable to describe the underlying data set. While there is no guarantee of a function that can be decomposed additively, the derived models effectively and accurately fitted the provided stress-strain responses despite the sparsity of the available data. Note, that enforcing this additive decomposition in the strain energy is possible. However, it would significantly constrain the search space.

3.3. Stretch-Based Model Identification

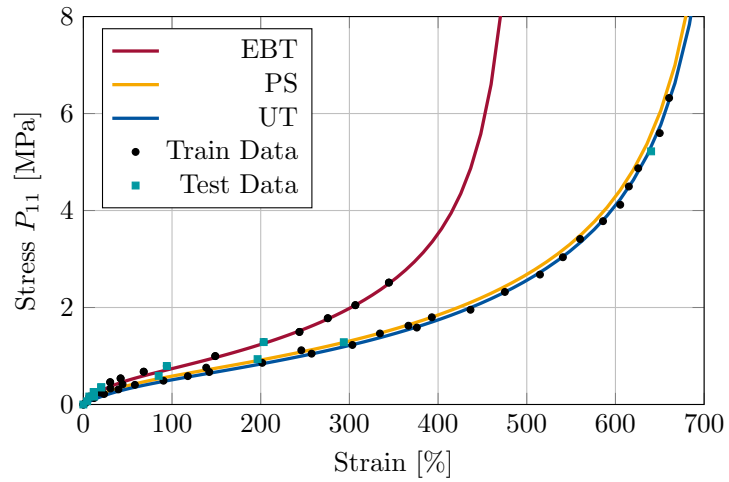
Could an alternative stretch-based formulation provides a simpler expression with less material parameters or a superior fit to the underlying data set using DSO? To be able to find the Ogden model we extended the initial set of functions by the power one ("pow"). Once again, an 80.00% to 20.00% train-test split was employed. Within the Valanis-Landel concept (8) the function ω was identified as follows:

$$\omega(\lambda) = 1.44 \left[0.4 \frac{2.96^\lambda}{\lambda} + \left(0.62 \sqrt{0.61\lambda + \sqrt{\exp\left(\frac{2.0^\lambda}{\lambda}\right) - 1}} \right)^{0.65} \right]^{0.4}. \quad (17)$$

The stress-strain response of the data set resulting from this function is illustrated in [Figure 7](#) against the experimental data by Treloar. R^2 score of 98.06% indicates that the identified strain energy function accurately predicts the responses for all three loading cases and exhibits a superior performance compared to the Ogden model ($R^2 = 95.58\%$). This example demonstrates the effectiveness of a stretch-based approach. While the degree of accuracy has been enhanced, the notable increase in complexity of the model represents however a significant drawback. One potential avenue for enhancing the simplicity of this approach is the incorporation of possible priors into the DSO framework. Thus, further investigations and detailed analysis are necessary to fully determine the potential of this approach.



(a)



(b)

Figure 6: Stress-strain responses of strain energy functions (15) and (16) against the experimental data by Treloar (1944) subject to two different levels of noise according to (14).

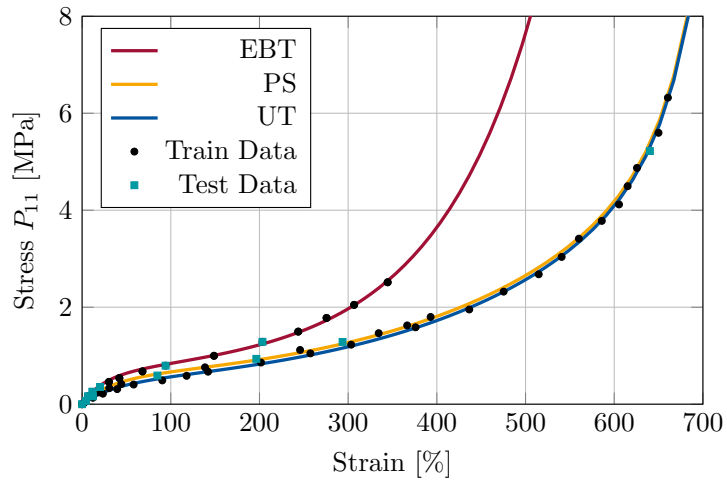


Figure 7: Stress-strain response of the stretch based model (17) against the Treloar data under UT, PS and EBT.

3.4. Biaxial Loading of Vulcanized Rubber

To evaluate the performance of the DSO package on the data set by Kawabata et al. (1981) from biaxial tension tests, three different training scenarios are explored. In the first scenario the UT, PS, and EBT responses are used to identify a strain energy function. The remaining data are used to evaluate the performance of the model, specifically its ability to predict the normal 1st Piola-Kirchhoff stresses in the loading directions 1 and 2 (P_{11} and P_{22}). Note that the stretch information λ_2 is only provided through the information of the first and second invariant and the assumption of incompressibility. In the second scenario, all data sets for the biaxial tension tests with various stretch relations are used to improve the performance of the model. The model is discovered only on the basis of P_{11} stress values. In the final scenario, the entire data set is used to evaluate the ability of the model to accurately predict all data points including the P_{11} and the P_{22} stresses. A test train split of 70.00 % to 30.00 % is applied for all three cases. Here, the strain energy function was determined as a function of the invariants I_C and II_C .

For the first example, the following strain energy is identified

$$\Psi_{K,1} = 0.43 \sqrt{\left(0.38 \left[I_C \left(0.30 I_C - 8.58 \times 10^{-4} II_C \ln II_C - 0.30 \ln I_C + 4.73 \right) + II_C \right] + 1 \right)}. \quad (18)$$

It demonstrates a high degree of agreement with the experimental data for UT, PS and EBT with R^2 score of 99.67 % as depicted in Figure 8a. Nevertheless, it is important to study how accurately the strain energy will predict responses in other scenarios.

In Figure 8b and Figure 8c the responses $P_{11}(\lambda_1)$ and $P_{22}(\lambda_2)$, respectively, are plotted for various values of λ_1 . Figure 8b demonstrates that these three loading cases are sufficient for characterizing the material behavior across various stretch combinations. However, P_{22} response which was not seen by DSO only qualitatively describes the experimental data. Thus, more information is need for more accurate stress predictions in the biaxial tension.

For the second training case the following strain energy is identified

$$\begin{aligned} \Psi_{K,2} = & 0.17 I_C - 0.03 + 0.10 \left(3.69 - 2.21 \sqrt{0.09 I_C - 0.20 \sqrt{II_C} + 1} \right) \\ & \cdot \ln \left(4.74 I_C + II_C + \ln \left(\sqrt{II_C} \right) + \frac{5.21}{I_C} \right). \end{aligned} \quad (19)$$

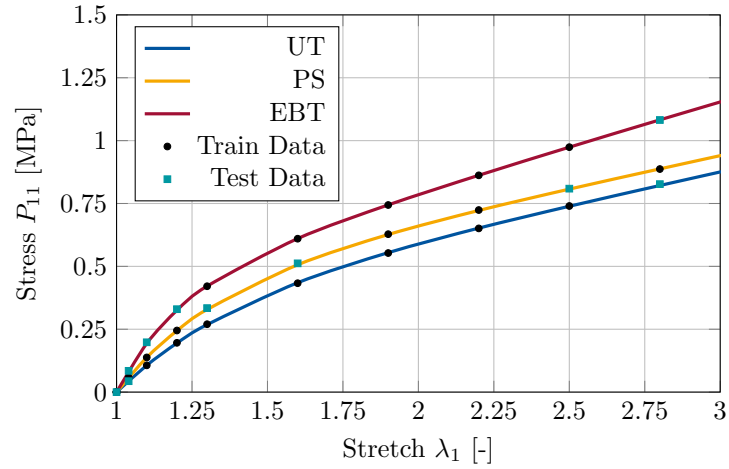
It achieved a R^2 score of 99.40 %. In this case, all data from the biaxial loading were utilized. However, only the P_{11} response was fitted, while the P_{22} response was excluded from the fitting process. The corresponding stress-strain responses are illustrated in Figure 9 against the experimental data by Kawabata et al. (1981). It is seen that the predictions based on (19) are very accurate for UT, PS and BT, effectively capturing all observed trends. However, the predictive accuracy of the model for P_{22} is less precise in comparison to P_{11} . In particular, P_{22} is considerably underestimated for $\lambda_1 = 3.7$. This indicates that both stresses are indispensable for the fitting.

In the final case, both P_{11} and P_{22} responses were used for the fitting. The strain energy was determined with

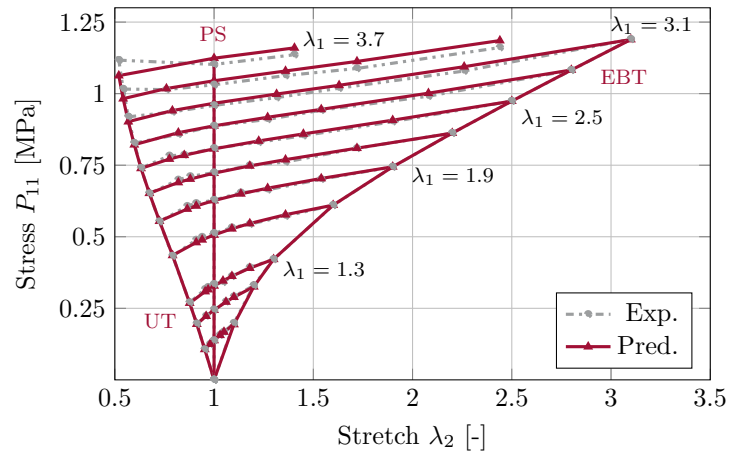
$$\begin{aligned} \Psi_{K,3} = & 0.12 I_C + 0.12 \sqrt{II_C} - 0.03 \ln II_C - 0.03 \ln \left(\ln (II_C)^4 \right) - 0.13 \\ & - \frac{0.03 (-3.49 I_C - 5.88 II_C) \ln (II_C)}{II_C}. \end{aligned} \quad (20)$$

The resulting responses are visualized in Figure 10. In this instance, the generated predictions are observed to be of an extremely high degree of accuracy with a R^2 score of 98.40 %. Nevertheless, due to the larger number of data points used compared to the second case, the accuracy is slightly lower. The fitting of both stress responses P_{11} and P_{22} has resulted in a notable enhancement in the precision of the calculated P_{22} response.

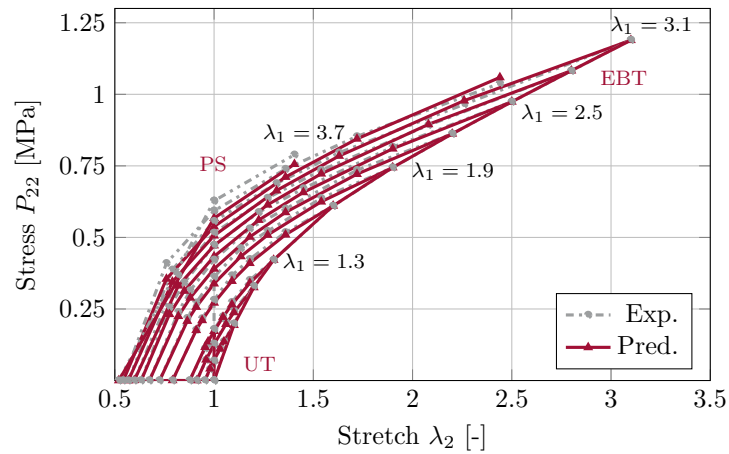
This analysis indicates that there is no single, universally applicable strain energy function, rather, multiple potential functions can adequately fit the same data set. The identified strain energy functions illustrate that both I_C and II_C , are indispensable as arguments of the strain energy function. In order to obtain a precise model capable of predicting a variety of loading scenarios, both the P_{11} and P_{22} responses are indispensable for the fitting process. While the experimental data obtained from UT, PS, and EBT experiments can yield satisfactory fits, it is crucial to acknowledge that these data may not provide highly accurate predictions for specific loading cases, particularly with regard to the P_{22} response. The P_{11} stress is sufficiently robust for the identification of a strain energy function which effectively captures the observed trends in the P_{22} response.



(a)

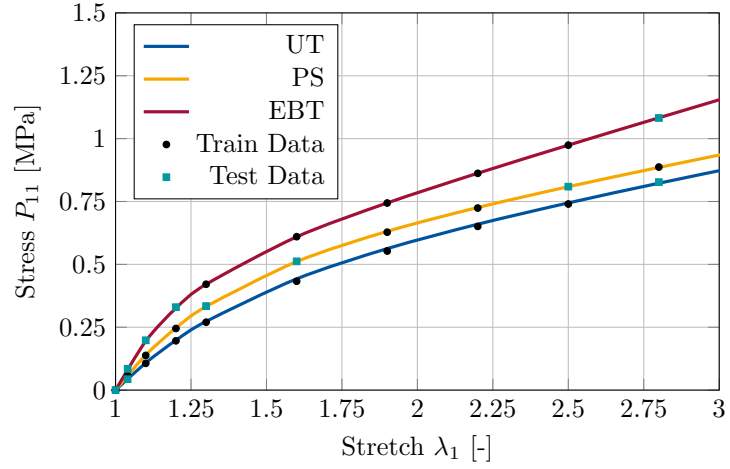


(b)

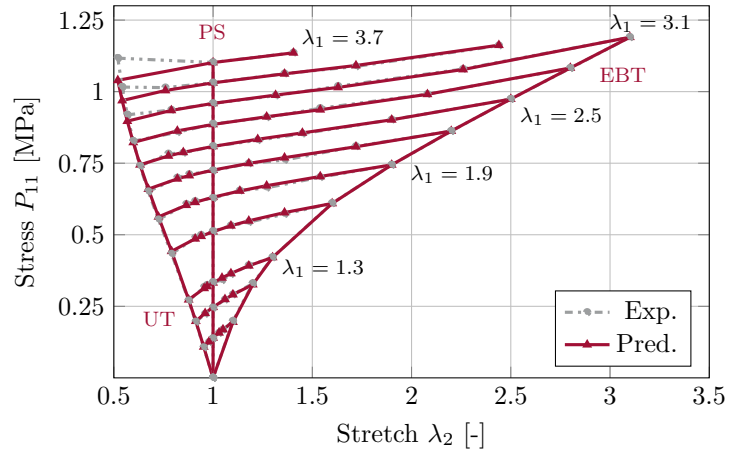


(c)

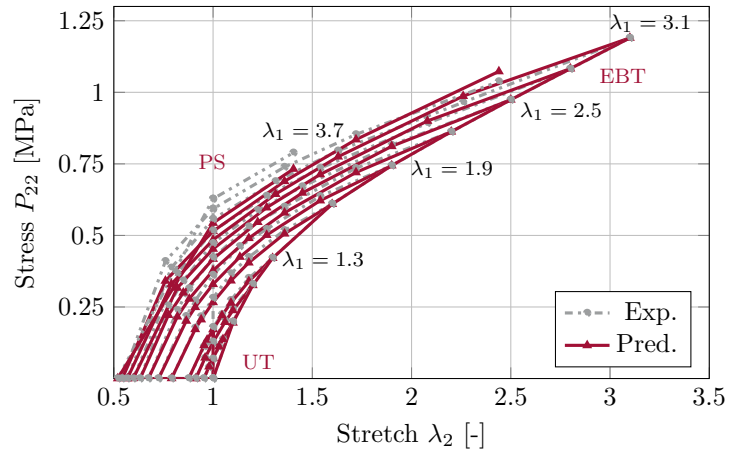
Figure 8: Stress-stretch responses (a) $P_{11}(\lambda_1)$ under UT, PS and EBT, (b) $P_{11}(\lambda_2)$ and (c) $P_{22}(\lambda_2)$ for different values of λ_{11} plotted against the experimental data by Kawabata et al. (1981). The responses result from the strain energy function (18) identified on the basis of P_{11} values from UT, PS and EBT.



(a)

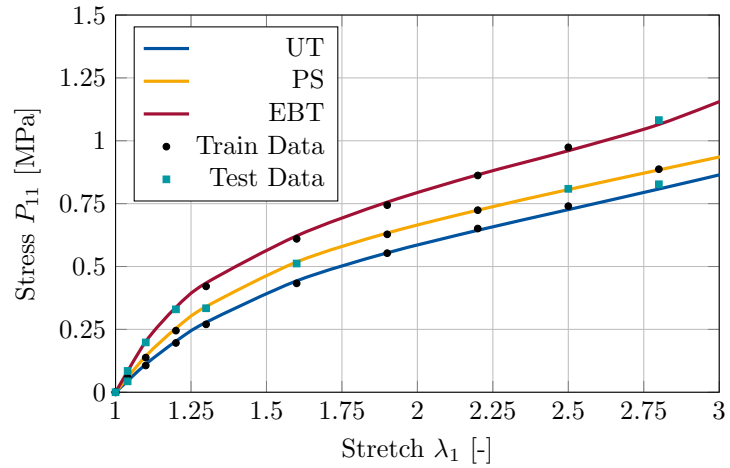


(b)

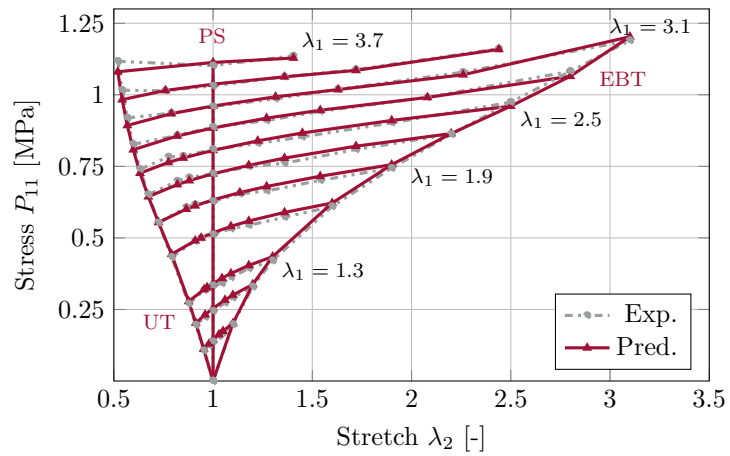


(c)

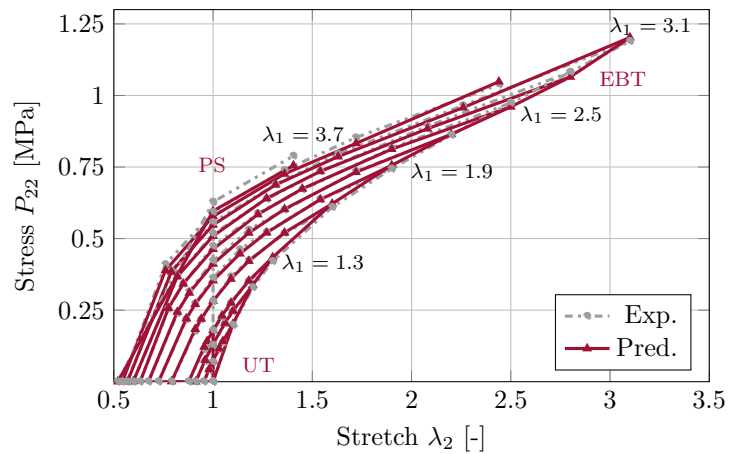
Figure 9: Stress-stretch responses (a) $P_{11}(\lambda_1)$ under UT, PS and EBT, (b) $P_{11}(\lambda_2)$ and (c) $P_{22}(\lambda_2)$ for different values of λ_{11} plotted against the experimental data by Kawabata et al. (1981). The responses result from the strain energy function (19) identified on the basis of P_{11} values from UT, PS and EBT.



(a)



(b)



(c)

Figure 10: Stress-stretch responses (a) $P_{11}(\lambda_1)$ under UT, PS and EBT, (b) $P_{11}(\lambda_2)$ and (c) $P_{22}(\lambda_2)$ for different values of λ_{11} plotted against the experimental data by Kawabata et al. (1981). The responses result from the strain energy function (20) identified on the basis of P_{11} values from UT, PS and EBT.

4. Conclusion

In this study, we have proposed a novel methodology that employs deep symbolic regression to derive interpretable hyperelastic material models for rubber-like materials under multi-axial loading conditions. By directly utilizing experimental data from the classical Treloar and Kawabata data sets, our methodology effectively identifies strain energy functions that not only accurately fit the data but also require few material parameters. This approach has been subjected to rigorous testing both invariant and stretch-based formulations using UT, PS and EBT data. In conclusion, the present study demonstrates the considerable potential of integrating deep symbolic regression with a continuum mechanical framework, even when data is limited. The important advantage of the proposed procedure is that it bypasses human bias in the model selection, thus more effectively capturing the complex behavior of rubber-like materials. Furthermore, the proposed methodology demonstrates robustness against data noise and versatility in predicting responses across various loading scenarios. The symbolic character of the identified model allows to analyze and interpret the contribution of each terms under different deformation modes. Domain-specific priors incorporated into the DSO framework will further be able to restrict the search space and simplify the resulting models.

References

- Abdolazizi, K.P., Aydin, R.C., Cyron, C.J., Linka, K., 2025. Constitutive kolmogorov-arnold networks (ckans): Combining accuracy and interpretability in data-driven material modeling. *arXiv preprint arXiv:2502.05682*.
- Abdusalamov, R., Hillgärtner, M., Itskov, M., 2023. Automatic generation of interpretable hyperelastic material models by symbolic regression. *International Journal for Numerical Methods in Engineering* 124, 2093–2104.
- Abdusalamov, R., Weise, J., Itskov, M., 2024. Rediscovering the mullins effect with deep symbolic regression. *International Journal of Plasticity* 179, 104037.
- Augusto, D., Barbosa, H., 2000. Symbolic regression via genetic programming, in: *Proceedings. Vol.1. Sixth Brazilian Symposium on Neural Networks*, pp. 173–178.
- Birky, D., Emery, J., Hamel, C., Hochhalter, J., 2025. Learning implicit yield surface models with uncertainty quantification for noisy datasets. *Computer Methods in Applied Mechanics and Engineering* 436, 117738.
- Bomarito, G., Townsend, T., Stewart, K., Esham, K., Emery, J., Hochhalter, J., 2021. Development of interpretable, data-driven plasticity models with symbolic regression. *Computers & Structures* 252, 106557.
- Dal, H., Açıkgöz, K., Badienia, Y., 2021. On the performance of isotropic hyperelastic constitutive models for rubber-like materials: A state of the art review. *Applied Mechanics Reviews* 73, 020802.
- Flaschel, M., Kumar, S., De Lorenzis, L., 2023. Automated discovery of generalized standard material models with euclid. *Computer Methods in Applied Mechanics and Engineering* 405, 115867.
- Fuhg, J.N., Padmanabha, G.A., Bouklas, N., Bahmani, B., Sun, W., Vlassis, N.N., Flaschel, M., Carrara, P., Lorenzis, L.D., 2024. A review on data-driven constitutive laws for solids. [arXiv:2405.03658](https://arxiv.org/abs/2405.03658).
- Gent, A.N., Thomas, A., 1958. Forms for the stored (strain) energy function for vulcanized rubber. *Journal of Polymer Science* 28, 625–628.
- He, H., Zhang, Q., Zhang, Y., Chen, J., Zhang, L., Li, F., 2022. A comparative study of 85 hyperelastic constitutive models for both unfilled rubber and highly filled rubber nanocomposite material. *Nano Materials Science* 4, 64–82.
- Herrmann, L., Kollmannsberger, S., 2024. Deep learning in computational mechanics: a review. *Computational Mechanics* 74, 281–331.
- Itskov, M., Knyazeva, A., 2016. A rubber elasticity and softening model based on chain length statistics. *International Journal of Solids and Structures* 80, 512–519.
- Kalina, K.A., Linden, L., Brummund, J., Kästner, M., 2023. Fe ann: an efficient data-driven multiscale approach based on physics-constrained neural networks and automated data mining. *Computational Mechanics* 71, 827–851.
- Kaliske, M., Heinrich, G., 1999. An extended tube-model for rubber elasticity: statistical-mechanical theory and finite element implementation. *Rubber Chemistry and Technology* 72, 602–632.
- Kawabata, S., Matsuda, M., Tei, K., Kawai, H., 1981. Experimental survey of the strain energy density function of isoprene rubber vulcanizate. *Macromolecules* 14, 154–162.
- Khiêm, V.N., Itskov, M., 2017. An averaging based tube model for deformation induced anisotropic stress softening of filled elastomers. *International Journal of Plasticity* 90, 96–115.
- Kirchdoerfer, T., Ortiz, M., 2016. Data-driven computational mechanics. *Computer Methods in Applied Mechanics and Engineering* 304, 81–101.
- Kissas, G., Mishra, S., Chatzi, E., De Lorenzis, L., 2024. The language of hyperelastic materials. *Computer Methods in Applied Mechanics and Engineering* 428, 117053.
- Klein, D.K., Fernández, M., Martin, R.J., Neff, P., Weeger, O., 2022. Polyconvex anisotropic hyperelasticity with neural networks. *Journal of the Mechanics and Physics of Solids* 159, 104703.
- Linka, K., Hillgärtner, M., Abdolazizi, K.P., Aydin, R.C., Itskov, M., Cyron, C.J., 2021. Constitutive artificial neural networks: A fast and general approach to predictive data-driven constitutive modeling by deep learning. *Journal of Computational Physics* 429, 110010.
- Linka, K., Kuhl, E., 2023. A new family of constitutive artificial neural networks towards automated model discovery. *Computer Methods in Applied Mechanics and Engineering* 403, 115731.
- Mahnken, R., 2022. Strain mode-dependent weighting functions in hyperelasticity accounting for verification, validation, and stability of material parameters. *Archive of Applied Mechanics* 92, 713–754.
- Marckmann, G., Verron, E., 2006. Comparison of hyperelastic models for rubber-like materials. *Rubber chemistry and technology* 79, 835–858.

- Melly, S.K., Liu, L., Liu, Y., Leng, J., 2021. A review on material models for isotropic hyperelasticity. *International Journal of Mechanical System Dynamics* 1, 71–88.
- Meng, S., Imtiaz, H., Liu, B., 2021. A simple interpolation-based approach towards the development of an accurate phenomenological constitutive relation for isotropic hyperelastic materials. *Extreme Mechanics Letters* 49, 101485.
- Miehe, C., Göktepe, S., Lulei, F., 2004. A micro-macro approach to rubber-like materials—part i: the non-affine micro-sphere model of rubber elasticity. *Journal of the Mechanics and Physics of Solids* 52, 2617–2660.
- Mirzapour, J., 2023. A micro-mechanically-based constitutive model for hyperelastic rubber-like materials considering the topological constraints. *International Journal of Solids and Structures* 275, 112299.
- Ogden, R.W., 1972. Large deformation isotropic elasticity—on the correlation of theory and experiment for incompressible rubberlike solids. *Proceedings of the Royal Society of London. A. Mathematical and Physical Sciences* 326, 565–584.
- Petersen, B.K., Landajuela, M., Mundhenk, T.N., Santiago, C.P., Kim, S.K., Kim, J.T., 2021. Deep symbolic regression: Recovering mathematical expressions from data via risk-seeking policy gradients.
- Richter, H., 1948. Das isotrope elastizitätsgesetz. *ZAMM-Journal of Applied Mathematics and Mechanics/Zeitschrift für Angewandte Mathematik und Mechanik* 28, 205–209.
- Ricker, A., Wriggers, P., 2023. Systematic fitting and comparison of hyperelastic continuum models for elastomers. *Archives of Computational Methods in Engineering* 30, 2257–2288.
- Rivlin, R.S., Saunders, D., 1951. Large elastic deformations of isotropic materials vii. experiments on the deformation of rubber. *Philosophical Transactions of the Royal Society of London. Series A, Mathematical and Physical Sciences* 243, 251–288.
- Shariff, M.H.B.M., 2000. Strain Energy Function for Filled and Unfilled Rubberlike Material. *Rubber Chemistry and Technology* 73, 1–18.
- Treloar, L.R., 1944. Stress-strain data for vulcanized rubber under various types of deformation. *Rubber Chemistry and Technology* 17, 813–825.
- Valanis, K., Landel, R.F., 1967. The strain-energy function of a hyperelastic material in terms of the extension ratios. *Journal of Applied Physics* 38, 2997–3002.
- Xiang, Y., Zhong, D., Rudykh, S., Zhou, H., Qu, S., Yang, W., 2020. A review of physically based and thermodynamically based constitutive models for soft materials. *Journal of Applied Mechanics* 87, 110801.